Giant thermal transport tuning at a metal/ferroelectric interface

Y.P. Zang[1,&], C. Di[1,&], Z. M. Geng[1], X. J. Yan[1,*], D.X. Ji[1], X.Y Jiang[1], H.Y. Fu[1], J.J. Wang[2], W. Guo[1], H.Y. Sun[1], L. Han[1], Y. L. Zhou[1], Z.B. Gu[1], D. Kong[1], H. Aramberri[3], C. Cazorla[4], J. Íñiguez[3,5], R. Rurali[6], L.Q. Chen[2], J. Zhou[1], D. Wu[1], M. H. Lu[1,*], Y.F. Nie[1,*], Y. F. Chen[1] & X.Q. Pan[7]

[1] National Laboratory of Solid State Microstructures, Jiangsu Key Laboratory of Artificial Functional Materials, College of Engineering and Applied Science and Collaborative Innovation Center of Advanced Microstructures, Nanjing University, Nanjing 210093, China

[2] Department of Materials Science and Engineering, Pennsylvania State University, State College, Pennsylvania 16802, United States

[3] Materials Research and Technology Department, Luxembourg Institute of Science and Technology (LIST), Avenue des Hauts-Fourneaux 5, L-4362 Esch/Alzette, Luxembourg

[4] Departament de Física, Universitat Politècnica de Catalunya, Campus Nord B4-B5, E-08034 Barcelona, Spain

[5] Department of Physics and Materials Science, University of Luxembourg, 41 Rue du Brill, L-4422 Belvaux, Luxembourg

[6] Institut de Ciència de Materials de Barcelona, ICMAB–CSIC, Campus UAB, 08193 Bellaterra, Spain

[7] Department of Chemical Engineering and Materials Science and Department of Physics and Astronomy, University of California, Irvine, 916 Engineering Tower, Irvine, California 92697, USA

[&] These authors contributed equally to this work.

[*] Electronic address: xjyan@nju.edu.cn, luminghui@nju.edu.cn and ynie@nju.edu.cn

Interfacial thermal transport plays a prominent role in the thermal management of nanoscale objects and is of fundamental importance for basic research and nanodevices[1,2]. At metal/insulator interfaces, a configuration commonly found in electronic devices, heat transport strongly depends upon the effective energy transfer from thermalized electrons in the metal to the phonons in the insulator. However, the mechanism of interfacial electron-phonon coupling and thermal transport at metal/insulator interfaces is not well understood. Here, we report the observation of a substantial enhancement of the interfacial thermal transport and the important role of surface charges at the metal/ferroelectric (Al/BiFeO$_3$) interface. By applying uniaxial strain, the interfacial thermal resistance can be varied substantially (up to an order of magnitude), which is attributed to the renormalized interfacial electron-phonon coupling caused by the charge redistribution due the polarization rotation at the interface. These results imply that surface charges at a metal/insulator interface can substantially enhance the interfacial electron-phonon-mediated thermal coupling, providing a new route to optimize the thermal transport performance in the next generation nanodevices, power electronics and thermal logic devices.

The manipulation of ~~the~~ heat flux <u>through nanostructures</u> and ~~the~~ dynamical tuning <u>of the</u> thermal properties of functional materials ~~and nanostructures~~ are critical issues ~~for~~ <u>in</u> both basic research and <u>electronic</u> applications ~~in electronics~~[1-4]. ~~For instance, h~~High thermal conductivity materials<u>, for example,</u> are desirable for electronic chips to promote heat dissipation and keep a low thermal budget[2,5], while materials with as small as possible thermal conductivity can be used to achieve high thermoelectric figures of merit[6]. As the miniaturization of electronic devices continues, fascinating

thermal behavior may emerge such as materials exhibiting negligible thermal resistance and phonons propagating ballistically[7-10]. In the nanoscale realm, thermal resistance is dominated by the scattering of phonons at boundaries[11]; hence, the conversion efficiency between heat energy carriers at the interfaces becomes very important[12]. Since electrons and phonons dominate heat conduction in metals and insulators[8,13], respectively, energy transfer must occur between them to allow heat transport across metal–insulator interfaces. Such electron (in metal)-phonon (in insulator) coupling can be either in an indirect or direct manner[13]. In the indirect case, electron-phonon coupling takes place in the metal side and a subsequent coupling between the phonons in the metal and in the insulator is required, just like in a junction between two insulators[14]. In the direct case, the electron-phonon coupling occurs between the free electrons in the metal and the phonons in the insulator. However, the mechanisms of underlying such interface electron-phonon couplings and how to improve the interface thermal conductivity is are yet not well understood up to date thus hindering the tuning of interface thermal conductivity.

The design of materials with desirable tailored thermal transport properties has been intensively investigated received tremendous attention in recent years, with the result that and there are many conventional methods to engineer the many thermal conductivity engineering methods now are well established, including including chemical element modification[15], superlattices[7,9], crystal structure optimization[16], and domain wall or grain boundary density controlling in ferroelectrics[17-22]. Much attention recognition has been paid given to the tuning of interfacial thermal transport tuning through homojunctions via chemical bonding modification[23], surface roughness engineering[24] or the insertion of buffer layers to promote interfacial heat

fluxes[25]. However, analogous investigations Ffor metal/ferroelectric interfaces, however, the investigation is are rather limited, despite of their abundance in novel electronic devices like thin film nanocapacitors[26], nanoscale ferroelectric memories[26,27] and magnetic/ferroelectric tunnel junctions[28,29]. Devising novel strategies to enhance the efficiently tunninginterfacial thermal transfer and effective tuning of the interfacial thermal resistance in of metal/ferroelectric interfaces, therefore, is pressingly needed.

In this work, we synthesize freestanding $BiFeO_3$ (BFO) films and deposit an aluminum metal layer on top of them to fabricate metal/ferroelectric interfaces and thus explore their interfacial thermal transport properties under uniaxial strain. By time domain thermoreflectance (TDTR) measurements, we observed an extremely high tunability of the thermal transport across the Al/BFO interface, as a that results from of the strain-driven rotation of the polarization in the ferroelectric $BiFeO_3$ layer, which modifies the electron-phonon coupling at the metal/ferroelectric interface.

As shown in Fig. 1, freestanding BFO films were synthesized by using $SrTiO_3$ (STO) as the substrate and water soluble $Sr_3Al_2O_6$ (SAO) as the sacrificial layer, as reported it has been previously reported[30-32]. Freestanding BFO films were transferred onto a flexible substrate (Poly-Ethylene-Naphthalte, PEN) by using epoxy as the glue, and the flexible PEN substrate was mounted on a stretching stage to apply uniaxial strain[33]. For thermal transport measurements, an aluminum layer was deposited on the films to form an Al/BFO/Epoxy/PEN heterostructure. Schematics of the sample transfer and uniaxial strain manipulation of the freestanding BFO films are shown in Figs. 1a & 1b. The topography of the freestanding BFO films on PEN exhibits high quality surface

showing clear atomic step-and-terraces (Fig. 1c and Fig. S1b).

In our experiments, we apply uniaxial strain along the high symmetry [100] pseudo-cubic direction to explore its impact on the thermal transport properties. In principle, one expects that by applying uniaxial strain along [100], the lattice will expand along the stretched direction and shrink along the other two perpendicular dimensions, as indeed is experimentally confirmed by our *in situ* x-ray diffraction measurements (Fig. 1c). Uniaxial strain along the BFO [100] axis can be continuously increased up to around 3.5% (above this point the material starts to relieve stress by forming microcracks). Raw data of high-resolution x-ray diffractions as a function of strain are provided in the Supplementary Information (Fig. S3).

The ferroelectric polarization of BFO films strongly relies on the lattice structure[34]. Epitaxial biaxial strain has been demonstrated to drive BFO films into tetragonal, rhombohedral and orthorhombic structures[35]. Recent progress in the synthesis of freestanding oxide films enables unprecedented freedom in engineering the materials' symmetry, strain and strain gradient for novel properties[33,36,37]. By taking the lateral piezoelectric force microscopy (LPFM) images with different rotation angles between the BFO films and cantilever, the polarization vector mapping can be extracted, showing that the polarization along the stretching direction increases under uniaxial strain (Fig. 2). (More detailed information on the LPFM and data analysis can be found in the Methods section and Supplementary Information (Fig. S4).) This observation is expected as the polarization of ferroelectric perovskites has the tendency to align with the elongated axis. For example, ~~this is the case of the~~ a phase transition from the rhombohedral "R-phase" (with polarization along a [111] direction)

to the tetragonal "T-phase" (with polarization along [001]) can be driven in BiFeO$_3$ films ~~driven~~ by the elongation of the out-of-plane c lattice ~~constant~~ parameter under compressive epitaxial strain[35]. Both the clear elongation of the in-plane lattice and prominent depolarization field in thin films tends to drive the polarization towards the stretching in-plane direction, which is consistent with our PFM measurements. The polarization rotation observed here is also similar to the one recently reported for PbTiO$_3$[38].

Thermal transport properties are measured by the TDTR method based on a pump and probe technique, as schematically shown in Fig. 3a. An aluminum metal layer is deposited on the suspended BFO ~~suspended~~ film to absorb the energy from the pump beam and generate heat. (The Al capping layer does not obviously affect the actual strain achieved in the BFO films under stretching, as shown in Supplementary Information Fig. S5.)~~.~~ The time resolved reflection signal of the probe beam reflects the thermal dissipation capability, from which the thermal transport properties of the material can be extracted. More details ~~about~~ of our TDTR measurements are ~~given~~ provided in the Methods section and Supplementary Information (Figs. S6-S7). As shown in Fig. 3b, the measured thermal resistance of the unstrained Al/BFO interface (obtained with ultrathin BFO films) in Al/BFO/Epoxy/PEN is 0.012 m^{2}K/MW. Remarkably, when tensile strain is applied, the thermal resistance ~~increases~~ substantially increases up to, ~~reaching~~ a maximum of 0.308 m^{2}K/MW at 3.5% uniaxial tensile strain, ~~with~~ which represents an enhancement of ~~an~~ one order of magnitude, ~~which is even higher than that~~ and surpasses the gain previously determined for the Bi/H-diamond interface[39]. Upon a further increase of the strain, the thermal resistance decreases again due to the relaxation of uniaxial stress and

appearance of microcracks. The variation of the thermal resistance is also reflected in the slope of the fitting curve (Fig. S6h). This general trend and the coincident sudden change in the thermal resistance and lattice parameters (XRD measurements) of BFO imply that the thermal resistance variation is correlated with the effective strain and lattice deformation. Repeated TDTR measurements show similar results (Fig. S8), indicating the reproducibility and robustness of the result. Note that the difference in nominal strain and variable quantity of thermal conductivity between Fig. S8 and Figure 3b is related to different production batches of epoxy. As shown in Fig. 3c, the TDTR measurement on Al/Epoxy/PEN –a similar structure, but without BFO film– does not show any strain dependence of the thermal resistance (Curve fitting shown in Fig.S9), thus implying that the giant thermal resistance change is related to the presence of BFO and rules out the influence caused by elastic piezoreflectance effects in polymers[40].

We now discuss the possible underlying mechanisms of underlying the giant strain-driven giant tunability of thermal transport in Al/BFO. There are several possible explanations: 1) It is The observed thermal resistance effects are related to the variation of the domain wall density in BFO films. since dDomain walls have been are believed to scatter phonons and affect the thermal transport properties in of ferroelectrics[17]. 2) As uniaxial strain is applied on the BFO films, the crystal structure distortion and polarization rotations may result in strong anisotropy of the thermal conductivity in BFO films. 3) It is The observed thermal resistance effects are related to the Al/BFO interface thermal resistance. T because the strain-driven BFO polarization rotation in BFO alters the density of bound charges at the interface, which may affect the interfacial electron-phonon coupling and interface thermal

1   resistance.

2

3   The first two mechanisms can be ruled out by experimental evidences and theoretical

4   calculations. First, as shown in Fig. 2a-b and Fig. S10 in the Supplementary

5   Information, PFM measurements show that the domain wall density only slightly

6   increases under strain. This also agrees with our phase-field simulations, which show

7   little differences between the domain wall density of strained and unstrained BFO

8   (Supplementary Information, Fig. S11). Second, first-principles theoretical

9   calculations show that changes in the thermal conductivity, κ, induced by uniaxial

10   strains of up to 6% are less than 2% (Supplementary Information, Fig. S12). They

11   also reveal that, as regards thermal conductivity, the anisotropy of rhombohedral (R3c)

12   bulk BFO is almost negligible and barely amounts to 3% (Fig. S12), thus a simple

13   strain-driven rotation of the lattice cannot explain by itself the observed effect (~~-~~in

14   contrast, see Ref.[41] for a strong anisotropy effect in PbTiO$_3$). Similar conclusions can

15   be drawn if we assume that upon strain BFO becomes super-tetragonal ~~with an~~

16   ~~increase in~~ and its anisotropy increases. The reduction ~~of~~ in thermal conductivity ~~due~~

17   ~~to this~~ resulting from such ~~increased~~ anisotropy increase may be ~~is~~ at most of 20%,

18   which is again too small to explain our observations (see the Methods section for full

19   details on the calculations). It is worth noticing that within the same computational

20   setup we predict a thermal conductivity for unstrained R3c BFO that is in excellent

21   agreement with the experimental observations[16], which confirms the reliability of our

22   first-principles results. Furthermore, previous experimental works on the "T-phase"

23   and "R-phase" of BFO also show small κ differences between them [16].

24

25   As a result, the giant tuning of the thermal conductance that we measured is most

likely related to the Al/BFO (metal/ferroelectric) interface. As discussed above, the thermal energy carried by the electrons in Al must be transferred to the phonons in BFO through direct electron-phonon coupling between the metal and ferroelectric or by electron-phonon coupling in Al followed by ~~a~~ subsequent phonon-phonon interaction across the interface. Note that there is an insulator/insulator interface (BFO/Epoxy) in addition to the Al/BFO interface~~;~~ however, ~~O~~our TDTR experiments show that the impact of the polarization switching on the interfacial thermal conductivity at ferroelectrics/epoxy interface is negligible (Supplementary information Fig. S16).

~~In~~ For the interface between a metal and an ionic insulator, the former mechanism – i.e., direct coupling between metallic charges and phonons in the oxide – is expected to be dominant[42]. If the ionic insulator is a ferroelectric oxide, and especially if the spontaneous polarization (or at least a component of it) is perpendicular to the metal/ferroelectric interface, this mechanism can be expected to be even more prevalent. In such a case, free charges accumulate on the metallic side of the interface to compensate (screen) the bound charge associated with the spontaneous polarization. Likewise, the natural thermal fluctuations of the polarization (which can be seen as a very strongly polar phonon pointing at the interface) effectively generates an oscillating electric field that couples to the screening charges (and, more generally, to the surface plasmons of the metal), which in turn couple to the electrons in the bulk of the metal. Then, strain (or an external electric field) can alter the distribution of polarization bound charges and metal screening near the interface, thus modifying the corresponding direct electron-phonon coupling. In particular, when the polarization rotates and lies in-plane, there is ~~no~~ neither a permanent accumulation of free charges

at the interface, nor a large and oscillating polarization coupled to them; hence, we can expect a smaller coupling with the surface plasmon on the metal side. (Our first-principles simulations of a Al/BFO interface system in which the BFO polarization was oriented along several directions, provide numerical evidence for smallest accumulation of interface screening charges in the metallic Al side when the BFO polarization is oriented parallel to the Al/BFO interface –see Fig. S17–.) It follows then that the direct electron-phonon coupling should becomes less efficient and consequently the thermal resistance of the interface should increase.

This scenario is formally described within the theory developed by Mahan for metal/polarinsulator interfaces[42], when the latter are *polar*. Therein, the thermal resistance of the interface reads as $r_i = (\sigma_0 \mathcal{I})^{-1}$, where σ_0 is a constant that depends on properties of the two bulk materials and on the system geometry, and can in principle can be considered independent of the possible spontaneous polarization of the insulator. $\mathcal{I}$, on the other hand, is an integral function that depends proportionally on the ionic charges near the interface and inversely on the dielectric constant of the insulator. Ferroelectrics are characterized by very large ionic (bound) charges associated with their spontaneous polar distortion; hence, if the ferroelectric polarization points towards the interface, this will contribute to a large value of $\mathcal{I}$ and, thus, a small thermal resistance (Figure 4c). Note also that our first-principles calculations indicate that the anisotropy of the dielectric constant (and thus of the screening) is not substantial in BFO. Hence, $\mathcal{I}$ is essentially controlled by the orientation of the polarization with respect to the metal/ferroelectric interface. In particular, the rotation of the polarization away from the interface should result in reduced interfacial bound charges, thus a reduced $\mathcal{I}$ and an increased thermal

1   resistance, exactly as observed.

2

3   To further confirm the fact that interfacial thermal transport can be tuned by changing

4   the orientation of the ferroelectric polarization, we performed TDTR experiments on

5   other metal/ferroelectric interfaces, namely, $Al/LiNbO_3$ and $Al/BaTiO_3$, where

6    $LiNbO_3$ (LNO) and $BaTiO_3$ (BTO) are single crystals in a nearly ferroelectric

7   monodomain state. Interfaces with various polarization orientation are explored by

8   deposi~~t~~ing the Al film on different surfaces of the crystals with ~~the~~ same surface

9   smoothness and quality (Fig. 4a-b). As shown in Fig. 4a, when the polarization is

10   lying in-plane, the interface thermal resistance of Al/LNO is increased by nearly a

11   factor of 3 as compared to the case with perpendicular upward polarization, which

12   ~~presents the same~~ is consistent with the trend ~~as~~ observed ~~at~~ for the Al/BFO

13   interface. As expected, the ~~amount of the~~ size of the interface thermal resistance

14   increase is smaller in this case because the experiments were performed for a bulk

15   crystal~~,~~ rather than for ultrathin membranes, and thus the relative weight of the

16   interface contribution to the overall thermal resistance is lower. Interestingly, the

17   interface thermal resistance ~~with~~ corresponding to the polarization pointing towards

18   the interface is lower than that ~~for~~ to the polarization pointing away from the interface.

19   This is most likely because ~~the~~ a higher density of free electrons is accumulated at the

20   interface ~~can further facilitate the interfacial thermal transfer~~ when the polarization is

21   pointing towards the interface. Since it is ~~more~~ very difficult to prepare ideal

22   monodomain BTO crystals, our BTO crystal presents mixed in-plane and out-of-plane

23   polarizations (Supplemental Information Fig. S14). Nonetheless, the polarization

24   along the out-of-plane direction is a single phase, thus allowing for the comparison of

25   the interface thermal resistance between the upward and downward polarization

configurations:, which actually confirms the results actually coincide with those obtained for observed at the Al/LNO interface. Data fitting and ratio sensitivity of TDTR measurement for LNO and BTO are shown in Fig. S15.

In conclusion, we report the observation of an unusually large modulation ofon the thermal transport across metal/ferroelectric interfaces by applying uniaxial strain to engineer the polarization orientations in the ferroelectric layer. Our results reveal an appealing physical picture that the interface bound charges have a drastic effect on the electron-phonon-mediated thermal coupling between the metal and the insulator layers. Electron–phonon interactions haves been shown to alter bulk phonon heat transport[43], but here we report an unprecedented and, most importantly, dynamically tunable heat resistance interface effect. This exceptionally large strain-thermal effect is of great interest for fundamental investigations and technological applications, as it demonstrates selective opening of an interface heat dissipation channel by rotating the polarization. Our work thus provides a new mechanism to optimize the thermal management of in the next- generation nanodevices, power electronics and thermal logic devices. For example, by using ferroelectric materials as in the insulatingon layers, or just simply by depositing a ferroelectric thin layers of ferroelectric film to bridge the heat transfer between the metal and insulatingion layers, may promote thermal dissipation in nanochips and power electronics. As the interfacial ferroelectric polarization may be switched by strain, external electric field or laser pumping, a metal/ferroelectric interface can also be potentially used in technologies related to ultra-sensitive thermal management and thermal logic devices.

METHODS SUMMARY

Epitaxial film growth , transfer and structure characterizations. We prepared the multiferroic $BiFeO_3$ and water-soluble sacrificial SAO films by Oxide Molecular Beam Epitaxy (OMBE). Firstly, (001) orientated SAO films were deposited on (001) orientated STO substrate at 850 °C with O^2 partial pressure of 1.29E-9 torr, then the BFO films were grown on SAO at 380 °C in ozone atmosphere with the partial pressure of ozone of 3.5E-8 torr. The detailed description of film preparation is described in our previous report[31].

In order to apply uniaxial strain, the BFO film is transferred to the flexible substrate Poly-Ethylene-Naphthalte (PEN). Epoxy adhesive is applied in order to improve the bonding force between the film and PEN. The specific film transfer process is shown in the Fig. 1a: First, a thin layer of epoxy is applied on the BFO film and then the PEN is attached on the top surface of the epoxy. Next, the sample was heated at 100°C for 0.5 hour to cure the epoxy. Then, the cured sample is dipped into water to dissolve the SAO film, which typically takes 2 days. When the SAO film is completely dissolved, the substrate can be removed easily, leaving the final BFO/Epoxy/PEN sample for measurements. Uniaxial strain is applied on the PEN using a homemade stretching setup. As shown in Supplementary Information Fig. S1-S3, the quality of the film and evolution of the lattice parameters under strain were measured by XRD, X-ray reflection (XRR) and reciprocal-space mapping (RSM), which is operated on a Bruker D8 Discover X-ray diffractometer.

Piezo response force microscopy measurements and data processing. The topography and ferroelectric properties of strained BFO films on a flexible PEN were measured by Asylum Research MFP-3D Origin+. In order to apply an electric field

effectively, a conductive carbon layer is coated on the backside of the PEN. Considering both the amplitude and phase data of a specific position at different sample rotation angles, we can derive a series of projection (signed values) varied with sample rotation angles, which can be fitted well by a sine function. Thus, the polarization state of each point in the overlapping area can be determined by the polarization and phase shift of the fitting curve[44]. Then we divide 360° into eight directions uniformly (each one occupies 45°, according to the polarization of $BiFeO_3$) and classify the in-plane polarization direction. The polarizations are represented by different colors, the final treated polarization diagrams are shown in Fig. 2c.

Time domain thermoreflectance (TDTR) measurements. Thermal dissipation capacity of the freestanding BFO films was characterized by the TDTR method. TDTR is a method suitable for measuring thermal properties of thin film materials and the fundamental principle of the method has been described elsewhere[23]. Mechanism explanation of TDTR measurement is shown in Fig. 3a. The incoming laser is divided into pump beam and probe beam by a polarizing beam splitter. The amplitude of the pump beam was modified as radio frequency sine wave, and the intensity of the probe beam was modified by a chopper. Then the path of the pump beam was tuned continuously by the delay stage, which allows delays with 0-4 nanoseconds. The pump beam irradiates on the surface of the sample, generating the heat, and the heat can be transferred down into the sample. The surface temperature of the material is related to its thermal conductivity, which affects the reflection efficiency of the probe beam. Thus, the thermal conductivity of the material can be obtained from the reflection signal of the probe beam. The pump beam was modulated at 9.8 MHz and the probe beam was chopped at 180 Hz to improve the signal-to-noise

1 ratio. The powers are 30 mW and 15 mW for the pump and probe, respectively. In this

2 work, the freestanding BFO films were supported by epoxy and a ~80nm Al film was

3 deposited onto the samples by magnetron sputtering to serve as heat transducer. It is

4 noteworthy that owing to the limited thickness of the BFO film (5.2nm by XRR), the

5 BFO film was treated as part of the interface, while bulk thermal conductivity of Al

6 and epoxy were included in the data fitting. All the fitting parameters, including

7 specific heat and thermal conductivity of Al, BFO, BTO, LNO and epoxy are obtained

8 from the homepage of the group of David. G. Cahill (https://cahill.matse.illinois.edu)

9 or literature[45-48]. The thermal resistance of BFO films and thermal conductivity of

10 epoxy are fitting parameters in the processing of data.

11

12 **Phase field simulations.** The phase-field method is employed to study the strain

13 effect on the domain structures and the corresponding effective thermal conductivity.

14 In the phase-field model of ferroelectric thin film, the polarization field $\mathbf{P}$ is selected

15 as the order parameter to describe the domain structures[49].

16

17 The spatial and temporal evolution of the polarization under external thermal, electric,

18 and mechanical stimuli is controlled by the time-dependent Ginzburg-Landau (TDGL)

19 equation,

20 $$\frac{\partial \mathbf{P}(x,t)}{\partial t} = -L \frac{\delta F}{\delta \mathbf{P}(x,t)},$$ (1)

21 where L represents the kinetic coefficient related to the domain wall mobility. The

22 total free energy in Eq.(1) includes contributions from the bulk chemical energy (f_{bulk}),

23 polarization gradient energy (f_{grad}), electric energy (f_{electric}), and elastic energy (f_{elastic}),

24 i.e.,

25 $$F = \iiint_V \left[f_{\text{bulk}}(\mathbf{P},T) + f_{\text{grad}}(\nabla \mathbf{P}) + f_{\text{electric}}(\mathbf{P},\mathbf{E}) + f_{\text{elastic}}(\mathbf{P},\boldsymbol{\varepsilon}) \right] dV,$$ (2)

1   where ε, $\mathbf{E}$, $\nabla \mathbf{P}$ represent the strain tensor, electric field vector, and polarization

2   gradient, respectively. One can also include other contributions such as chemical

3   potentials of charged defects and flexoelectric coupling in Equation (2). The

4   expressions of each energy term can be found in previous review papers[49]. The

5   electric-field and stress distributions coupled with the domain structures are

6   determined by solving the electrostatic equilibrium equation with short-circuit electric

7   boundary condition and elastic equilibrium equation with strained boundary condition,

8   respectively. A system size of $200\Delta x \times 200\Delta x \times (N_{\text{Substrate}}+N_{\text{BFO}}+N_{\text{Air}})\Delta z$ with

9   $\Delta x=\Delta z=1$nm, $N_{\text{Substrate}}=12$, $N_{\text{BFO}}=10$, and $N_{\text{Air}}=4$ is employed to do the phase-field

10 simulations of domain structures. Material parameters of $BiFeO_3$ used in the

11 simulation are taken from the literature[50]. To calculate the effective thermal

12 conductivity of different domain structures, the heat conduction equation is solved

13 $$\frac{\partial}{\partial x_i}\left(k_{ij}(\boldsymbol{x})\frac{\partial T(\boldsymbol{x})}{\partial x_j}\right) + q(\boldsymbol{x}) = \rho c_p \frac{\partial T(\boldsymbol{x})}{\partial t}, \tag{3}$$

14 where $k_{ij}(\mathbf{x})$ is the spatial-dependent thermal conductivity tensor, $T(\mathbf{x})$ is the

15 temperature distribution, ρ, c_p, and $q(\mathbf{x})$ are the mass density, specific heat capacity,

16 and the internal heat source of the material, respectively. The spatially dependent

17 thermal conductivity in a ferroelectric thin film with domain structure then can be

18 described as follows[51].

19 $$k_{ij}(\boldsymbol{x}) = k_{ij}^{\text{fs-wall}}\eta(\boldsymbol{x}) + k_{ij}^{\text{domain}}\big(1 - \eta(\boldsymbol{x})\big), \tag{4}$$

20 where $k_{ij}^{\text{fs-wall}}$ and k_{ij}^{domain} represent the individual thermal conductivity of the

21 ferroelastic domain wall and domain, respectively. In the simulation, we assume the

22 domain and domain walls thermal conductivities of 1.0 $Wm^{-1}K^{-1}$ and 0.1 $Wm^{-1}K^{-1}$,

23 respectively, arising from their different phonon scattering abilities observed in

24 experiments[17,18]. The heat conduction equation is solved using a spectral iterative

perturbation method, which can be found in the literature[51].

First principles calculations of the thermal conductivity of BFO. We computed the second- and third-order interatomic force constants (IFCs) within density-functional theory as implemented in the VASP code[52], using the local density approximation for the exchange-correlation energy functional and a plane-wave cutoff of 500 eV with the projector augmented-wave method[53]. The IFCs are calculated from finite differences and the inequivalent displacements were generated with the PHONOPY[54] and THIRDORDER.PY[55] codes. We used a $3 \times 3 \times 3$ and a $2 \times 2 \times 2$ supercell of the rhombohedral primitive cell for the second- and third-order IFCs, respectively.

In the case of an applied strain of 6% we considered the experimental lattice parameters. We started with a 40-atom cell where it is easy to impose the pseudo-cubic lattice parameters. With this distortion of the cell and a full optimization of atomic positions and cell angles, we obtain a structure that, provided that we accept deviations of 0.1 Å, has a Cc symmetry, which corresponds to a 20-atom unit cell. For this unit cell we computed both the second- and third-order IFCs in a $2 \times 2 \times 2$ supercell.

The computed IFCs are used as inputs to solve the linearized phonon Boltzmann Transport Equation (BTE) using the iterative method implemented in the SHENGBTE code[55]. The lattice thermal conductivity is obtained as

$$\kappa^{\alpha\beta} = \frac{1}{k_B T^2 VN} \sum_\lambda f_0(f_0+1)(\hbar\omega_\lambda)^2 v_\lambda^\alpha F_\lambda^\beta, \qquad (5)$$

where α and β are the three coordinate directions x, y, and z; and k_B, T, V, and N are the Boltzmann constant, the temperature, the volume of the unit cell, and the number

of $\mathbf{q}$ points, respectively. The sum runs over all the phonon modes λ, which have wave-vector $\mathbf{q}$ and branch ν. f_0 is the equilibrium Bose-Einstein distribution function, $\hbar$ is the reduced Planck constant, and ω_λ and v_λ^α are the phonon frequency and phonon group velocity. F_λ^β is initially taken to be equal to $\tau_\lambda v_\lambda^\beta$, where τ_λ is the lifetime of the phonon mode λ within the Relaxation Time Approximation (RTA). The BTE was solved on a $10 \times 10 \times 10$ and a $3 \times 5 \times 4$ grid of $\mathbf{q}$-points for the unstrained R3c and strained Cc case, respectively.

Additionally, we simulated a Al/BFO interface system in which the electric polarization of the BFO layer was forced to be oriented along (1) the pseudocubic [110] direction, which is parallel to the Al/BFO interface, and (2) the pseudocubic [111] direction, which is not parallel to the Al/BFO interface (Fig. S17). The Al region contained a total of 72 atoms and was ~18 Å thick, while the BFO region contained a total of 152 atoms and was ~27 Å thick. The fcc lattice parameters and atomic positions in the Al region were adjusted to minimize the strain at the Al/BFO interface, while the lattice parameters and atomic positions in the BFO region were kept fixed in order to constrain the direction and size of the corresponding polarization. Periodic boundary conditions were applied along the three lattice vectors defining the simulation supercell. Planar and macroscopic average potentials were then estimated along the direction perpendicular to the Al/BFO interface for systems (1) and (2) in order to quantify the magnitude of the dipole moment created at the Al/BFO interface, which can be ascribed to the presence of bound charges in the ferroelectric BFO side and of free screening charges in the metallic Al side. Macroscopic average potentials were obtained by taking averages of the planar potential over distances of one unit

1   cell along the same direction.

2

References

1.   Ball, P. Feeling the heat. *Nature* **492**, 174-176, (2012).
2.   Li, S. *et al.* High thermal conductivity in cubic boron arsenide crystals. *Science* **361**, 579-581, (2018).
3.   Cui, L. J. *et al.* Thermal conductance of single-molecule junctions. *Nature* **572**, 628-+, (2019).
4.   Mosso, N. *et al.* Heat transport through atomic contacts. *Nat. Nanotechnol.* **12**, 430-433, (2017).
5.   Chen, S. S. *et al.* Thermal conductivity of isotopically modified graphene. *Nat. Mater.* **11**, 203-207, (2012).
6.   Vaziri, S. *et al.* Ultrahigh thermal isolation across heterogeneously layered two-dimensional materials. *Sci. Adv.* **5**, (2019).
7.   Luckyanova, M. N. *et al.* Coherent Phonon Heat Conduction in Superlattices. *Science* **338**, 936-939, (2012).
8.   Cheaito, R. *et al.* Experimental investigation of size effects on the thermal conductivity of silicon-germanium alloy thin films. *Phys. Rev. Lett.* **109**, 195901, (2012).
9.   Ravichandran, J. *et al.* Crossover from incoherent to coherent phonon scattering in epitaxial oxide superlattices. *Nat. Mater.* **13**, 168-172, (2014).
10.   Maldovan, M. Phonon wave interference and thermal bandgap materials. *Nat. Mater.* **14**, 667-674, (2015).
11.   Zardo, I. & Rurali, R. Manipulating phonons at the nanoscale: Impurities and boundaries. *Curr. Opin. in Green Sustain. Chem.* **17**, 1-7, (2019).
12.   Giri, A. & Hopkins, P. E. A Review of Experimental and Computational Advances in Thermal Boundary Conductance and Nanoscale Thermal Transport across Solid Interfaces. *Adv. Funct. Mater.* **30**, (2020).
13.   Majumdar, A. & Reddy, P. Role of electron-phonon coupling in thermal conductance of metal-nonmetal interfaces. *Appl. Phys. Lett.* **84**, 4768-4770, (2004).
14.   Swartz, E. T. & Pohl, R. O. Thermal-Boundary Resistance. *Rev. Mod. Phys.* **61**, 605-668, (1989).
15.   Cho, J. *et al.* Electrochemically tunable thermal conductivity of lithium cobalt oxide. *Nat. Commun.* **5**, (2014).
16.   Ning, S. *et al.* Dependence of the Thermal Conductivity of $BiFeO_3$ Thin Films on Polarization and Structure. *Phys. Rev. Appl.* **8**, (2017).
17.   Langenberg, E. *et al.* Ferroelectric Domain Walls in $PbTiO_3$ Are Effective Regulators of Heat Flow at Room Temperature. *Nano Lett.* **19**, 7901-7907, (2019).
18.   Hopkins, P. E. *et al.* Effects of coherent ferroelastic domain walls on the thermal conductivity and Kapitza conductance in bismuth ferrite. *Appl. Phys. Lett.* **102**, (2013).
19.   Mante, A. J. H. & Volger, J. Phonon Transport in Barium Titanate. *Physica* **52**, 577-&, (1971).
20.   Weilert, M. A., Msall, M. E., Anderson, A. C. & Wolfe, J. P.

Phonon-Scattering from Ferroelectric Domain-Walls - Phonon Imaging in Kdp. *Phys. Rev. Lett.* **71**, 735-738, (1993).

21   Ihlefeld, J. F. *et al.* Room-Temperature Voltage Tunable Phonon Thermal Conductivity via Reconfigurable Interfaces in Ferroelectric Thin Films. *Nano Lett.* **15**, 1791-1795, (2015).

22   Foley, B. M. *et al.* Voltage-Controlled Bistable Thermal Conductivity in Suspended Ferroelectric Thin-Film Membranes. *ACS Appl. Mater. Interfaces* **10**, 25493-25501, (2018).

23   Losego, M. D., Grady, M. E., Sottos, N. R., Cahill, D. G. & Braun, P. V. Effects of chemical bonding on heat transport across interfaces. *Nat. Mater.* **11**, 502-506, (2012).

24   Hopkins, P. E., Phinney, L. M., Serrano, J. R. & Beechem, T. E. Effects of surface roughness and oxide layer on the thermal boundary conductance at aluminum/silicon interfaces. *Phys. Rev. B* **82**, (2010).

25   English, T. S. *et al.* Enhancing and tuning phonon transport at vibrationally mismatched solid-solid interfaces. *Phys. Rev. B* **85**, (2012).

26   Dawber, M., Rabe, K. M. & Scott, J. F. Physics of thin-film ferroelectric oxides. *Rev. Mod. Phys.* **77**, 1083-1130, (2005).

27   Scott, J. F. Applications of modern ferroelectrics. *Science* **315**, 954-959, (2007).

28   Tsymbal, E. Y. & Kohlstedt, H. Applied physics - Tunneling across a ferroelectric. *Science* **313**, 181-183, (2006).

29   Garcia, V. *et al.* Giant tunnel electroresistance for non-destructive readout of ferroelectric states. *Nature* **460**, 81-84, (2009).

30   Lu, D. *et al.* Synthesis of freestanding single-crystal perovskite films and heterostructures by etching of sacrificial water-soluble layers. *Nat. Mater.* **15**, 1255-1260, (2016).

31   Ji, D. *et al.* Freestanding crystalline oxide perovskites down to the monolayer limit. *Nature* **570**, 87-90, (2019).

32   Xu, R. J. *et al.* Strain-induced room-temperature ferroelectricity in $SrTiO_3$ membranes. *Nat. Commun.* **11**, (2020).

33   Han, L. *et al.* Giant Uniaxial Strain Ferroelectric Domain Tuning in Freestanding $PbTiO_3$ Films. *Adv. Mater. Interfaces* **7**, (2020).

34   Jang, H. W. *et al.* Strain-induced polarization rotation in epitaxial (001) $BiFeO_3$ thin films. *Phys. Rev. Lett.* **101**, 107602, (2008).

35   Sando, D., Barthelemy, A. & Bibes, M. $BiFeO_3$ epitaxial thin films and devices: past, present and future. *J. Phys.: Condens. Matter* **26**, 473201, (2014).

36   Hong, S. S. *et al.* Extreme tensile strain states in $La_{0.7}Ca_{0.3}MnO_3$ membranes. *Science* **368**, 71-76, (2020).

37   Dong, G. H. *et al.* Super-elastic ferroelectric single-crystal membrane with continuous electric dipole rotation. *Science* **366**, 475-+, (2019).

38   Torres, P., Iniguez, J. & Rurali, R. Giant Electrophononic Response in $PbTiO_3$ by Strain Engineering. *Phys. Rev. Lett.* **123**, (2019).

39   Lyeo, H. K. & Cahill, D. G. Thermal conductance of interfaces between highly dissimilar materials. *Phys. Rev. B* **73**, (2006).

40   Wang, X. J., Ho, V., Segalman, R. A. & Cahill, D. G. Thermal Conductivity of High-Modulus Polymer Fibers. *Macromolecules* **46**, 4937-4943, (2013).

41   Seijas-Bellido, J. A., Iniguez, J. & Rurali, R. Anisotropy-driven thermal conductivity switching and thermal hysteresis in a ferroelectric. *Appl. Phys. Lett.* **115**, (2019).

42   Mahan, G. D. Kapitza thermal resistance between a metal and a nonmetal. *Phys. Rev. B* **79**, (2009).

43   Zhou, J. *et al.* Direct observation of large electron-phonon interaction effect on phonon heat transport. *Nat. Commun.* **11**, 6040, (2020).

44   Kim, J., You, M., Kim, K. E., Chu, K. & Yang, C. H. Artificial creation and separation of a single vortex-antivortex pair in a ferroelectric flatland. *npj Quantum Mater.* **4**, (2019).

45   Wang, Y. *et al.* First-principles lattice dynamics and heat capacity of $BiFeO_3$. *Acta Mater.* **59**, 4229-4234, (2011).

46   Strukov, B. A. *et al.* Specific heat and heat conductivity of $BaTiO_3$ polycrystalline films in the thickness range 20-1100 nm. *J. Phys.: Condens. Matter* **15**, 4331-4340, (2003).

47   Lin, F., Bhatia, G. S. & Ford, J. D. Thermal-Conductivities of Powder-Filled Epoxy-Resins. *J. Appl. Polym. Sci.* **49**, 1901-1908, (1993).

48   Yao, S. H. *et al.* Growth, optical and thermal properties of near-stoichiometric $LiNbO_3$ single crystal. *J. Alloys Compd.* **455**, 501-505, (2008).

49   Wang, J. J., Wang, B. & Chen, L. Q. Understanding, Predicting, and Designing Ferroelectric Domain Structures and Switching Guided by the Phase-Field Method. *Annu. Rev. Mater. Res.* **49**, 127-152, (2019).

50   Zhang, J. X., Schlom, D. G., Chen, L. Q. & Eom, C. B. Tuning the remanent polarization of epitaxial ferroelectric thin films with strain. *Appl. Phys. Lett.* **95**, (2009).

51   Wang, J. J., Wang, Y., Ihlefeld, J. F., Hopkins, P. E. & Chen, L. Q. Tunable thermal conductivity via domain structure engineering in ferroelectric thin films: A phase-field simulation. *Acta Mater.* **111**, 220-231, (2016).

52   Kresse, G. & Furthmuller, J. Efficient iterative schemes for ab initio total-energy calculations using a plane-wave basis set. *Phys. Rev. B* **54**, 11169-11186, (1996).

53   Blochl, P. E. Projector Augmented-Wave Method. *Phys. Rev. B* **50**, 17953-17979, (1994).

54   Togo, A. & Tanaka, I. First principles phonon calculations in materials science. *Scr. Mater.* **108**, 1-5, (2015).

55   Li, W., Carrete, J., Katcho, N. A. & Mingo, N. ShengBTE: A solver of the Boltzmann transport equation for phonons. *Comput. Phys. Commun.* **185**, 1747-1758, (2014).

Acknowledgements

## Author contributions

Y.F.N. conceived this work, and directed the project with the help of X.Q.P. and Y.F.C. Y.P.Z. synthesized the samples and characterized the crystalline structure with the help of D.X.J., H.Y.S. and W.G under the supervision of Y.F.N., X.Q.P. and Z.B.G. Sample stretching method was developed by Y.P.Z. with the help of D.S.K. and Y.L.Z. Y.P.Z. performed the PFM measurements and data analysis with the help of X.Y.J, H.Y.F., L.H. under the supervision of Y.F.N. and D.W. C.D. and Z.M.G. performed TDTR measurements under the supervision of Y.F.C., M.H.L and X.J.Y. J.J.W. was responsible for the phase field simulation under the supervision of L.Q.C. H.A., C.C., J.Í., and R.R. performed and interpreted the first-principles calculations. J.Z. helped with the discussion of the underlying mechanism. Y.F.N. and Y.P.Z. wrote the manuscript. All authors discussed the data and contributed to the manuscript.
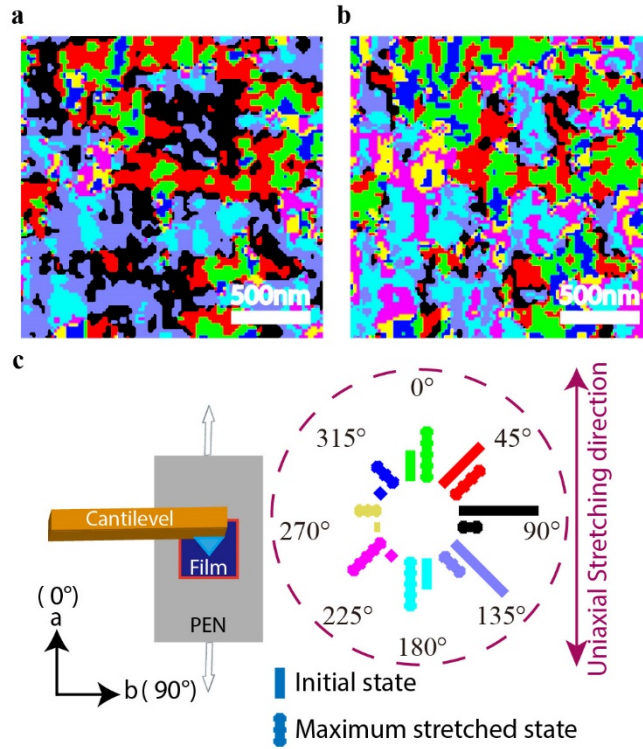
1   **Figures**

2
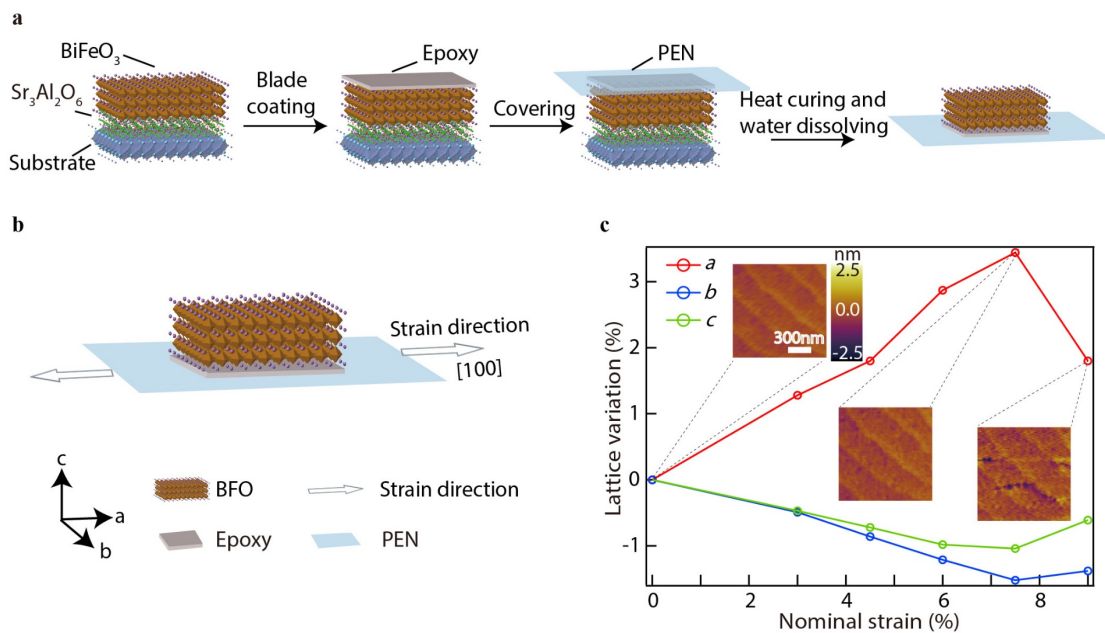
3
4

5   **Figure 1 Synthesis and uniaxial strain engineering of freestanding BiFeO$_3$ films.**
6   **a,** Schematic of the sample synthesis and transfer process of freestanding
7   BiFeO$_3$(BFO) films. The final BFO/Epoxy/PEN structure is used for uniaxial strain
8   experiments. **b**, Schematic of uniaxial stretching along the *a* axis. **c**, The lattice
9   variation of transferred BFO films (5.2 nm) under different nominal strain showing
10   the expansion of the lattice along the stretching direction and shrinkage along the
11   other two axes. After reaching a maximum expansion of about 3.5%, the film forms
12   microcracks and starts to relax. The inset topography images show a smooth step and
13   terrace surface of the film and the formation of microcracks under large strain. Lattice
14   strain is defined as $(L_x-L_0)/L_0$, where L_0 and L_x are the lattice constants under the
15   nominal strain of 0% and x%, respectively.
16

Figure 2 Evolution of the polarization in freestanding BFO films (5.2 nm) under uniaxial strain. **a-b**, In-plane domain structure measured by PFM polarization vector mapping for the bare freestanding BFO film under 0% (a) and 3.5% (b) uniaxial strain. **c**, Evolution of the domain volume projected along different in-plane directions showing the increase of the domains with polarization along the stretching direction. Left image shows the definition of azimuth angle between cantilever and sample stretching direction, right image represents the distributions of in-plane projected polarizations.
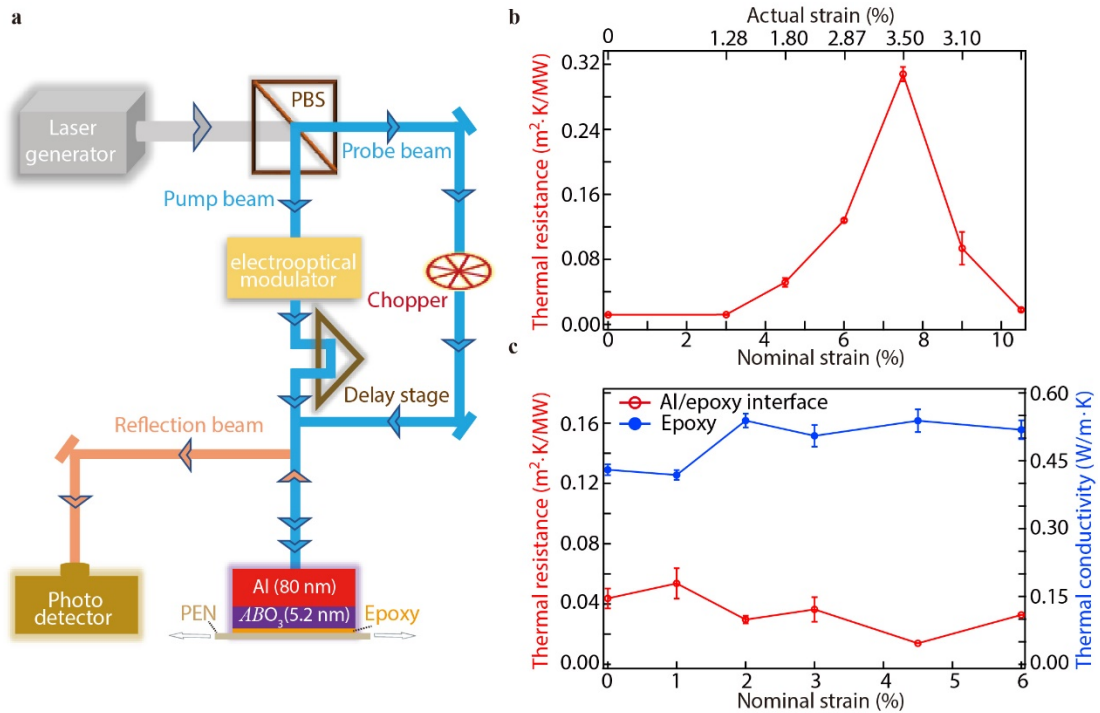
Figure 3 Thermal transport properties of Al/BFO measured by TDTR technique. a, Schematic of the TDTR technique based on a pump and probe technique. b, Thermal resistance of Al/BFO as a function of strain. It shows a drastic increase of the thermal resistance as strain increases and reaches a maximum value before the lattice starts to relax due to the formation of microcracks. c, Thermal resistance of Al/Epoxy interface (red line) and thermal conductivity of epoxy (blue line) have negligible variation under strain, indicating the strain dependent thermal resistance is related to Al/BFO interface.
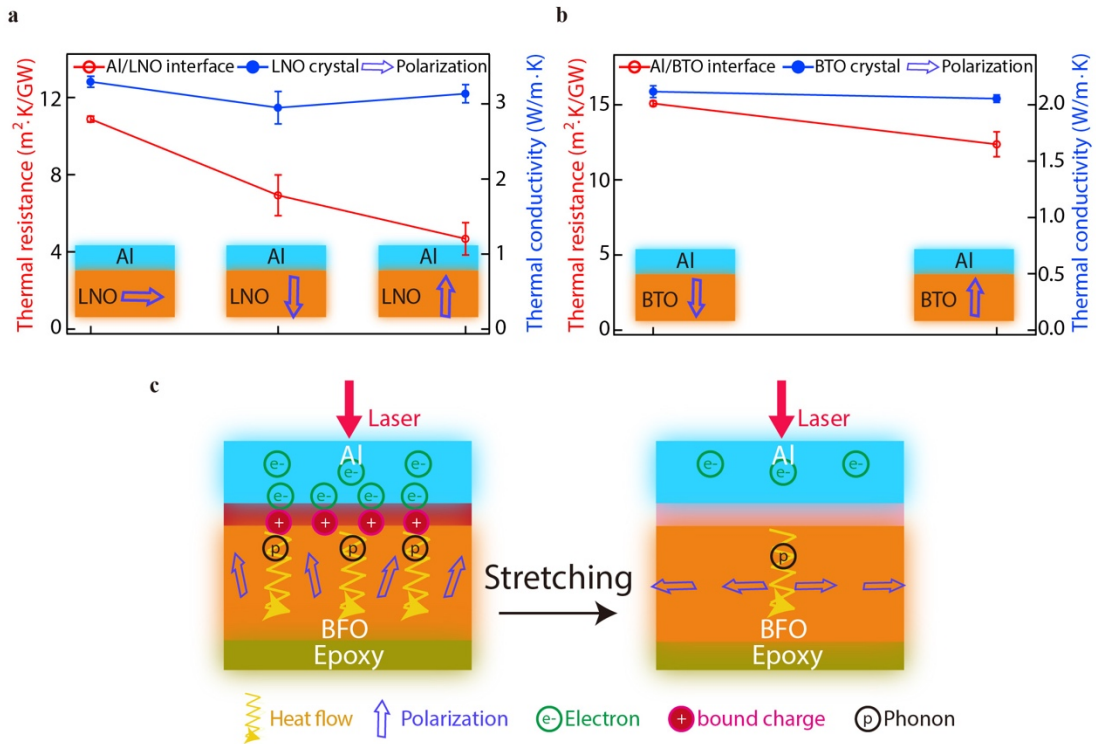
Figure 4 Strong dependence of the thermal resistance on the ferroelectric polarization orientation. a, Thermal resistance of Al/LiNbO$_3$ interface (red line) and thermal conductivity of LiNbO$_3$ crystal (blue line) measured by TDTR on LiNbO$_3$ crystals with different polarization orientations, showing the highest (lowest) thermal resistance at the interface with in-plane (upward) polarization. **b**, Thermal resistance of Al/ BaTiO$_3$ interface (red line) and thermal conductivity of BaTiO$_3$ crystal (blue line) measured by TDTR on BaTiO$_3$ crystals with different polarization orientations, showing higher (lower) thermal resistance at the interface with downward (upward) polarization. **c**, Schematic cartoon depicting the mechanisms of giant regulation of thermal transport by engineering the polarization orientation, density of bound charges and free electrons at the interface by applying uniaxial strain.